# Supported sodium aluminate catalysts effectively catalyze biodiesel synthesis

*Giovanni Pampararo[1]*, Damien P. Debecker[1]**

1. Université catholique de Louvain (UCLouvain), Institute of Condensed Matter and Nanosciences (IMCN), Place Louis Pasteur 1, Louvain-la-Neuve, 1348, Belgium

giovanni.pampararo@uclouvain.be; damien.debecker@uclouvain.be

KEYWORDS: $NaAlO_2$, Transesterification, DRIFTS, $CO_2$-TPD, Heterogeneous catalyst, Vegetable oil, Fatty acid methyl esters

**Abstract**:

Strongly basic sodium aluminate ($NaAlO_2$) was supported on titanium dioxide, γ-alumina, and hydrotalcite by impregnation. The resulting catalysts showed improved specific activity in the transesterification of sunflower oil in methanol, as compared to the unsupported $NaAlO_2$. Even with small sodium aluminate loading (i.e. 2.3% up to 9.4%) valuables fatty acid methyl esters (FAME) yields can be obtained. In particular, 9.4SA-HT shows the best catalytic activity achieving a 70% yield after 240 min of reaction, with a mere catalyst loading of 1.5% wt (with respect to the oil mass) in the reaction media. Innovatively, a detailed correlation between the amount, strength, and nature of the basic sites and the support type is proposed. In particular, it is demonstrated that only a part of the basic sites is effectively available for catalysis because of the already adsorbed atmospheric $CO_2$. Thus, a combination of effective availability and strength of the active species is pivotal for a high catalytic performance in the synthesis of biodiesel from triglycerides.

## 1. Introduction

In our society, transport remains largely related to fossil fuel combustion, and the derived gaseous emissions are damaging the environment as for example $CO_2$, $NO_x$, $SO_x$ and particulate emissions for the automotive sector [1,2]. In the last decades, important research efforts have been made to develop alternative fuels such as, for example, biofuels [3]. Among these, biodiesel can be obtained from the transesterification of bio-based fat (i.e. triglycerides) with methanol. The resulting fatty acid methyl ester (FAME) mix is a suitable fuel because it has lower overall exhaust emissions [4], it doesn't contain any sulfur compounds [5,6] and it has a superior flash point and biodegradability [7,8]. Furthermore, it can be industrially produced at low temperatures, with a homogeneous or a heterogeneous catalyst [9]. Industrially, the major technology is based on homogeneous catalysis (i.e. strong bases or strong acids), which comes with several drawbacks such as equipment corrosion, soap formation in the presence of moisture, neutralization costs for the large amount of wastewater [7,10].

"Several solid acid and basic catalysts have been developed for this reaction over the years, mainly based on group I and group II elements but also on transition metals [11–13]. Acid catalysts have also been investigated, mainly based on sulfated [14,15], sulfonated materials [16–18] or heteropoly acids [19]. Focusing on basic catalysts, many reports deal with KF/ZnO,[20] K-$Al_2O_3$,[21] K/$TiO_2$,[22] MgO-based catalysts,[23–25] and Ca-based catalysts [26,27]. Researchers have also applied tailored preparation routes to develop original biodiesel synthesis catalysts, such as for example formulations based on supported ionic liquids and magnetic $Fe_3O_4$ [28], supported heteropoly acids [29,30], carbon dots [31], alkali-doped MgO [32], $SrZrO_3$ [33], shaped ZnO nanoparticles [34], and porous Ca-Ce mixed oxides [35].

Nevertheless, despite the huge amount of literature that can be found on the topic, heterogeneous catalysis for biodiesel synthesis is not a breakthrough yet in industry [36]. In fact, although solid catalysts have favorable characteristics (such as recoverability and reusability) and perfectly match green chemistry principles, their preparation is often associated with non-cost-effective syntheses,

time consuming procedures that discourage a further development for the scale up. Actually, a truly active, robust and economic heterogeneous catalyst is yet to come.

We recently [37] demonstrated that sodium aluminate, $NaAlO_2$ (SA), could be a promising catalyst for biodiesel synthesis. It is strongly basic, cheap, and it doesn't leach in the reaction medium. Indeed, it outperformed strong and widely used heterogeneous basic catalysts such as CaO, Hydrotalcites, KI-$Al_2O_3$ or SrO, achieving almost 80% FAME yield after only 60 min. However, SA also features some drawbacks, such as its low specific surface area (which limits the amount of surface basic site per catalyst mass) and its reactivity with moisture (which complicates storage and handling). To solve these problems, a possibility is to disperse it on a suitable support. Despite the simplicity of this reasoning, only a handful of papers discussed this possibility [38–42]. Moreover, the effect of the nature of the support and the impact of SA loading onto the amount, strength, and nature of surface basic sites was not elucidated. Studies that relate catalytic functions to surface chemical properties are still needed in this domain.

In this work, we propose to investigate a series of hydrotalcite-, alumina- and titania-supported sodium aluminate catalysts with an active phase loading in the 2.3 – 9.4 wt.% range, and to elucidate the effect of the support on the resulting basic and textural properties. The latter are then correlated with catalytic performances, allowing us to propose a unified explanation on the catalytic behavior of these strongly basic materials.

## 2. Experimental Section

### *2.1 Catalysts synthesis*

Catalysts with various sodium aluminate (SA) contents have been synthesized by a wet impregnation (WI) technique. The selected supports are titanium dioxide (T, Degussa P25), Hydrotalcite (HT, Kisuma 4T-U), and γ-alumina (A, obtained by thermal transformation of commercial boehmite (Dequasol®, Dequachim)). All the supports were calcined before being impregnated: 2 °C/min up to

110 °C and dwell for 3 hours; then 5°C/min to 450 °C and dwell for 5 hours. To target nominal SA loadings of 2.3, 4.6, or 9.4 wt.%, the required amount of an aqueous sodium aluminate solution (Natral®, Sodium Aluminate wt 23%, Dequachim) was mixed with 10 mL of distilled water in a beaker, except in the case of $TiO_2$ where 25 mL have been employed. Then, 5 grams of calcined catalytic support was introduced to form a suspension that is progressively dried, under stirring, on a heating plate at 90 °C. The drying was completed overnight in an oven under static air, at 120 °C. The obtained powders were then calcined under static air conditions, in a furnace with the temperature program. The catalysts are denoted: xSA-T, xSA-A, and xSA-HT, where "x" represents the SA nominal weight loading, and where "T", "A", and "HT" denote the support used (titania, alumina, or hydrotalcite respectively).

### *2.2 Characterizations techniques*

X-Ray Diffraction (XRD) patterns were recorded using a Bruker D8 Advance diffractometer (Bragg–Brentano geometry). Cu is the Kα source (λ=0.15418 nm) at 1200 W (30 mA, 40 kV). The operative parameters are the following: 2θ range 10°-100°, step size 0.05° (2θ) and 1.5 s each step. The detector is a Bruker Lynxeye XE-T. The identification of the crystalline structures was carried out using the Pearson Crystal Database (PCD).

$N_2$ physisorption experiments were carried out at 77 K using a Micrometrics Tristar 3000 instrument. Prior to analysis, the calcined catalysts were degassed overnight under vacuum at 443 K. The Brunauer-Emmett-Teller (BET) model was used to calculate the specific surface area (SSA, $m^2/g$) in the relative pressure range of 0.05–0.30. Total pore volume ($V_p$) was estimated from the desorption branch of the isotherm at $p/p_0$=0.98 and the average pore diameter ($D_p$) was estimated from the BJH model applied on the desorption isotherms.

Fourier Transformed Infrared Spectroscopy (FT-IR) studies were carried out on a Bruker Equinox 55 spectrometer from 400 $cm^{-1}$ to 4000 $cm^{-1}$. Backgrounds were recorded in ambient air. The samples

were mixed and crushed with KBr (0.5 wt.% of catalyst in KBr) and pressed to produce wafers of 0.5 g. Spectra were collected, in the transmission mode, with 140 scans and a resolution of 4 $cm^{-1}$.

DRIFTS studies were performed on the same instrument. A background was collected before each measurement with an aluminum mirror. Before each measurement, catalysts were dried at 120 °C – then, a first spectrum has been recorded. Then, the sample was heated to 400°C in a He flow and held at this temperature for 1 h to remove weakly adsorbed species. After cooling to 60 °C, a 2$^{nd}$ DRIFT spectrum was recorded. The subtraction spectra reported and discussed below were obtained by subtracting the second recorded spectrum to the first one.

X-ray Photoelectrons Spectroscopy (XPS) analyses were carried out at room temperature with an SSI-X-probe (SSX 100/206) photoelectron spectrometer from Surface Science Instruments (USA), equipped with a monochromatic Al K X-ray micro focused source (1486.6 eV). Samples were deposited onto sample holders with adhesive tape and then placed on an insulating ceramic carousel (Macor®, Switzerland). Charge effects were avoided by placing a nickel grid above the samples and using a flood gun set at 8 eV. The binding energy scale was calibrated by fixing the C-(C,H) component of the C 1s peak at 284.8 eV. Data were analysed with the CasaXPS program (Casa Software Ltd., UK). The peaks were decomposed into a sum of Gaussian/Lorentzian (85/15) product function after subtraction of a Shirley-type baseline.

Carbon dioxide temperature-programmed desorption ($CO_2$-TPD) experiments were conducted on a CATLAB instrument (Hidden) equipped with a QGA mass spectrometer for gas analysis. The catalyst powder (85 mg) was introduced in a quartz reactor and degassed at 400 °C for 1h using a heating ramp of 10 °C/min in flowing helium (50 mL/min). Next, the sample was cooled to 60 °C and exposed to a 15% $CO_2$-Ar (50 mL/min) mixture for 90 min. The samples were finally purged in flowing Ar for 90 min at the same temperature. During the TPD experiments, the sample was heated from 60 °C to 800 °C using a heating rate of 5 °C/min, in an Ar flow of 50 mL/min. The amount of desorbed $CO_2$ was obtained by integration of the desorption profiles and referenced to the calibrated signals for

known volumes of analyzed gases. As a reference, $CO_2$-TPD was also performed without pretreatment, using the same procedure, but omitting degassing procedure (i.e. heating up to 400 °C prior to the $CO_2$ adsorption step, is not applied). In another variation of the experiment, the TPD step was interrupted at 400 °C (instead of 800 °C). In this case, the catalyst powder was stored in vacuum for further investigations (i.e. catalytic testing, see below).

ICP-AES analyses were carried out on an ICP Thermo Scientific 6500 instrument after dissolution of the catalyst (≃100 mg) in a metaborate solution ($LiBO_2$+$Li_2B_4O_7$).

### *2.3 Catalytic transesterification of sunflower oil*

Catalytic tests were carried out in batch, into a double necked 50mL flask. 150 mg of dried catalysts were introduced in the flask with 5.5 mL of methanol (Alfa Aesar, ≥ 99%), and the flask was placed in a silicon oil bath at 60 °C. The mixture was stirred at 450 rpm for 45 min to reach reflux conditions. In parallel, 10 g of commercial sunflower oil were heated at 100 °C for 45 min (to remove the moisture) and subsequently cooled to 60°C. Then, the oil was added to the MeOH/catalyst mixture and left reacting for 4h under vigorous stirring and reflux conditions. A sampling (equivalent to 100 mg), with a syringe, was applied at 20 min, 60 min, 120 min, 180 min and 240 min. Finally, the catalyst was separated from the liquid by centrifugation at 10,000 rpm for 10 min. For GC analysis, the reaction medium samples were processed as follows: 100 mg of the mixture was dissolved in 5 mL of n-Hexane (Roth, ≥ 99%) and 500 µL of the internal standard (Octyl acetate (Sigma Aldrich, ≥ 99%), $C_{is}$ =17 mg/mL) was added. 2.5 mL of the resulting solution were filtered and placed in dedicated GC vials.

The aliquots were analyzed with a Gas Chromatograph (GC-FID) Bruker SCION 456 equipped with an Agilent IU DB-FATWAX 30 m, 0.25 mm, 0.25 µm column. The injector temperature was set at 250 °C with a split ratio of 20. The oven temperature was raised with a 10 °C/min ramp from 150 °C

to 240 °C. FID temperature was set at 250°C. All the Fatty acid methyl esters (FAME) involved in the reaction were calibrated by using a FAME mixture (certified reference, F.A.M.E. Mix, C4-C24, Supelco) and calculating response factors. Consistent with the sunflower oil composition (according to the British Pharmacopoeia database, it contains palmitic acid (5%), stearic acid (6%), oleic acid (30%) and linoleic acid (59%)), the main detected peaks were: methyl palmitate (C17:0), Methyl palmitoleate (C17:1), Methyl stearate (C19:0), Methyl oleate/Methyl elaidate (C19:1n9 trans + cis) and Methyl linoleate/Methyl linolelaidate (C19:2n3 + C19:2n6) (see example of chromatogram in Fig. S0). The biodiesel yield was evaluated as follow:

FAME Yield (FY%) = $\Sigma$ ($Ci_{FAME}$) / $C_{mix}$

Where $Ci_{FAME}$ is the sum of all the methyl esters concentrations quantified via the chromatogram, $C_{mix}$ is the concentration of the reaction mix and it corresponds to 20 mg/mL. Every injection was repeated 3 times and values were averaged. Experimental relative error was evaluated at ~4%.

Leaching tests were carried out by rapidly removing the catalyst after 20 min of reaction, by means of 2 centrifugations at 10.000 rpm for 10 min. The catalyst-free mixture was then put again under reaction conditions (60 °C, stirring, reflux). After 60 min, 120 min, 180 min, and 240 min the mixture was sampled (100 mg) with a syringe and prepared to be analyzed via GC-FID with the previously described procedure.

Reusability tests have been carried out by running the reaction for 60 min, then separating the catalyst by centrifugation. The catalyst was washed three times with methanol and three times with n-hexane (5 mL each time) followed by filtration. The powder was either dried for two hours at 140 °C and tested again, or dried for 45 min at 140 °C, calcined at 450 °C for 60 min and tested again.

## 3. Results

### *3.1 Catalyst characterization*

ICP analyses (Table 1) revealed that the Na content was slightly and systematically lower than the theoretical values. This suggests that the actual precursor concentration in the impregnation process was slightly lower than announced by the manufacturer.

**Table1:** elemental analyses, specific surface area, and basic sites quantification (by $CO_2$-TPD).

| **Sample** | **$NaAlO_2$ %[a]** | **SSA ($m^2/g$) [b]** | **Pore volume ($cm^3/g$) [c]** | **Basic sites (mmol $CO_2/g_{cat}$)[d]** | | | **Total basic sites (mmol $CO_2/g_{cat}$)** |
|---|---|---|---|---|---|---|---|
| | | | | **Weak (0-400°C)** | **Medium (400-650°C)** | **Strong (650-800°C)** | |
| T | / | 40 | 0.17 | 0.017 | 0.007 | 0.005 | 0.029 |
| 2.3SA-T | 2.2 | 30 | 0.28 | 0.122 | 0.014 | 0.012 | 0.148 |
| 4.6SA-T | 3.9 | 25 | 0.35 | 0.244 | 0.116 | 0.025 | 0.385 |
| 9.4SA-T | 6.4 | 15 | 0.15 | 0.259 | 0.110 | 0.024 | 0.393 |
| A | / | 290 | 0.62 | 0.013 | 0.012 | 0.003 | 0.028 |
| 2.3SA-A | 2.3 | 210 | 0.42 | 0.126 | 0.018 | 0.016 | 0.16 |
| 4.6SA-A | 3.6 | 175 | 0.37 | 0.257 | 0.019 | 0.018 | 0.294 |
| 9.4SA-A | 6.6 | 110 | 0.26 | 0.390 | 0.148 | 0.055 | 0.593 |
| HT | / | 220 | 0.77 | 0.373 | 0.100 | 0.069 | 0.542 |
| 2.3SA-HT | 1.9 | 160 | 0.19 | 0.234 | 0.087 | 0.024 | 0.345 |
| 4.6SA-HT | 4.8 | 70 | 0.13 | 0.120 | 0.281 | 0.035 | 0.436 |
| 9.4SA-HT | 6.9 | 40 | 0.09 | 0.118 | 0.247 | 0.069 | 0.434 |

[a] wt % measured by ICP analysis, $NaAlO_2$ amount is calculated from Na content, and considering that all the Na is present in the form of $NaAlO_2$ [b] Specific Surface area calculated by means of BET method on adsorption branch [c] Average pore volume evaluated on the adsorbed volume plot; on the top of the isotherm at $p/p_0 = 0.98$ adsorption branch [d] evaluated by integrations of TPD profiles, the total is the mathematical sum reported in the last column.

XRD patterns for the studied catalysts are reported in Figure 1. The patterns of $TiO_2$ based catalysts showed the presence of both anatase tI12 (PCD n. 1960485) and tP6 rutile (PCD n. 1838255) crystalline phases. No peak related to $NaAlO_2$ oP16 (PCD n.313636) was found, even at the highest loading i.e. 9.4% wt. A similar situation was found in alumina-supported catalysts, where all the peaks present in the XRD patterns were attributable to $\gamma$-$Al_2O_3$ defective spinel cF56 (PCD n. 454845). In hydrotalcite-supported catalysts, the typical crystalline phase of calcined hydrotalcites (i.e. non-stoichiometric defective spinel, PCD n. 1932778) was detected. Interestingly, the pattern of 9.4SA-HT revealed a peak at $2\theta = 32.4$ ° that is attributable to a hydroxycarbonate with the similar structure of dawsonite $NaAl(OH)_2CO_3$ (PCD n. 1632877). In fact, although it is reported that dawsonite decomposes under 400°C [43], the release of $CO_2$ from its structure continues up to 650 °C, and it has been also studied as trapper for carbon dioxide [44]. Thus, it is possible that $CO_2$ is partially retained in a sort of partially crystalline hydrated carbonate. The peaks at $2\theta = 18.8$, 20.5, 38.1, already noticeable on 4.6SA-HT, can be assigned to the structures of the $NaAlO_2{*}5/4\ H_2O$ (PCD n. 1101228) and $Na_2O{*}Al_2O_3{*}2.5H_2O$ (PCD n.1729290). Although the hydrated form of $NaAlO_2$ normally decomposes after 150°C [45], its presence is related to the strong hygroscopic behavior of the material. Because the crystalline cell is the same, i.e. tP42, and the stoichiometry of the sample is complex, the presence of the mixed oxide phases cannot be excluded. Finally, no shift has been observed among the patterns of the support phases, meaning that the crystalline structure of the supports was not affected by the introduction of sodium aluminate.

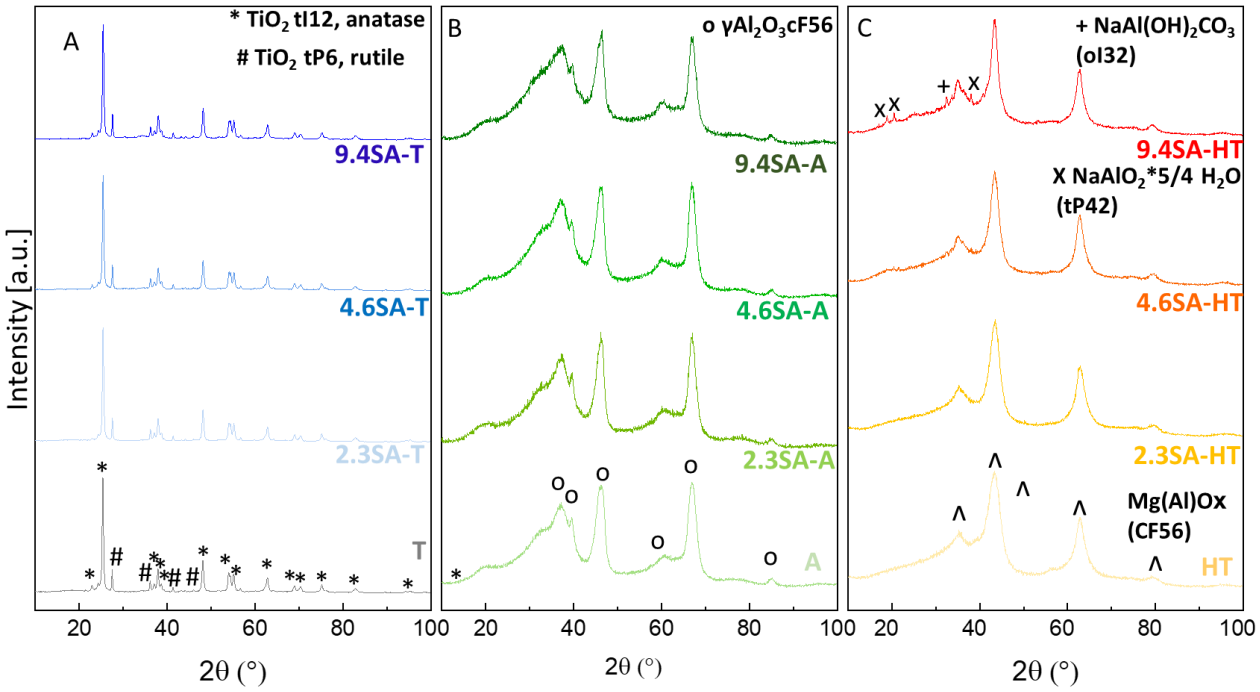


Figure 1: XRD patterns of calcined catalysts, panel A refers to titania-based catalysts, panel B refers to alumina-based ones and panel C refers to the hydrotalcite supported catalysts.

$N_2$ adsorption/desorption isotherms at 77 K and the corresponding BJH pore size distributions are shown in Figure 2. All isotherms exhibited a hysteresis loop and are conform to the IUPAC classification for mesoporous materials [46]. Titania based catalysts showed type IV isotherms with a H3 type hysteresis loop (appearing at $p/p_0$ = 0.85–1.0), suggesting the presence of slit-like pores resulting from interparticle voids [47,48]. Thus, the drop in specific surface area upon increasing the SA loading (see Table 1) was mainly due to the progressive filling of the interparticle space. Alumina-supported catalysts clearly showed type IV isotherms, with type H2 hysteresis loops, underlining complex pore structures strongly influenced by network effects. The steep desorption branch at $p/p_0$ = 0.65 is a feature that can be attributed to pore-blocking in a narrow range of pore necks (5.9-6 nm). The pore volume linearly decreased from 0.62 $cm^3/g$ to 0.26 $cm^3/g$ with the SA impregnation loading, indicating that the pores were progressively filled by the sodium aluminate. As reported in Table 1, the specific surface area (SSA) also progressively declined, and the pore diameter progressively decreased from 7 to 5 nm. Hydrotalcite-based catalysts showed type IV isotherms, and the pristine

support presented a H3 type hysteresis loop that is typical of non-rigid aggregates of plate-like particles and multimodal pore distribution (e.g. clays) [49]. Upon SA addition the loop turned into a H4 type that is typical for hierarchically porous materials [50,51]. In parallel, the SSA dropped markedly (Table 1) upon increasing the sodium aluminate loading. Accordingly, pore volume decreased from 0.77 $cm^3/g$ to 0.09 $cm^3/g$. Finally, a common feature is the abrupt hysteresis loop closing at $p/p_0 \sim$ 0.45, indicative of the tensile strength effect, and indicating the presence of pores smaller than 3.8 nm [52,53].

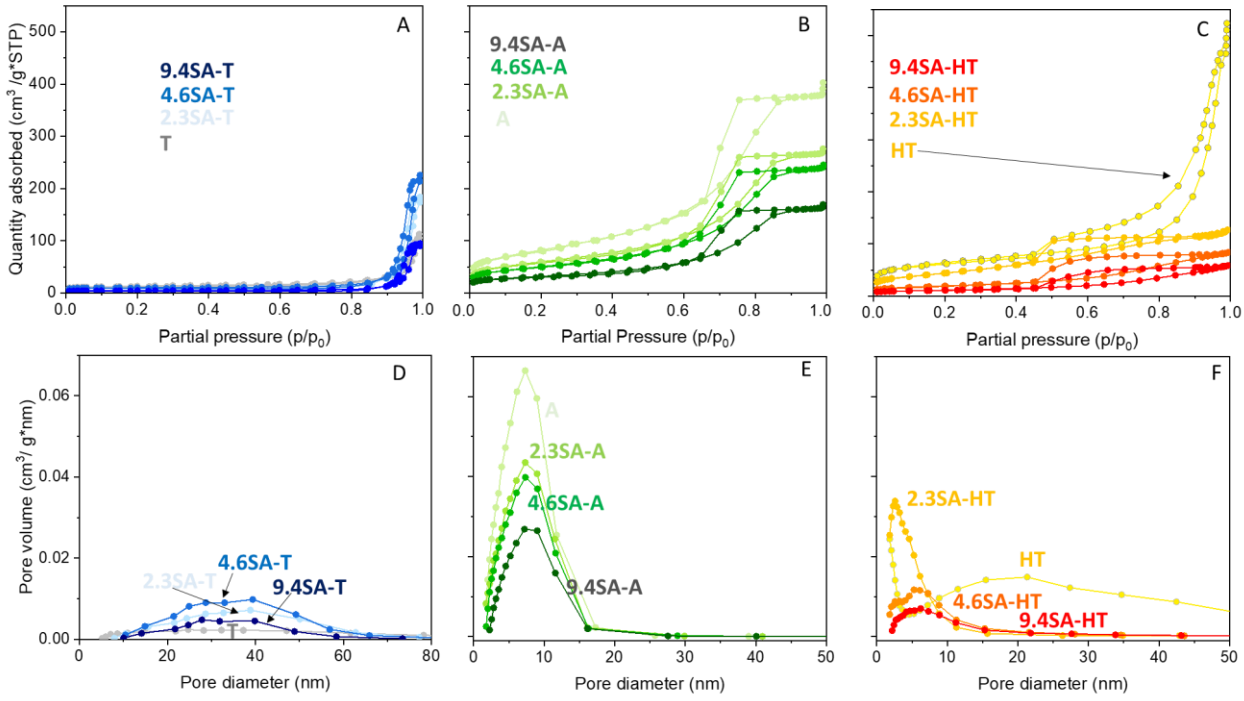


Figure 2: $N_2$ physisorption isotherms of the prepared catalysts (A, B, C) and pores size distributions (D, E, F) obtained via the BJH model applied on the adsorption isotherms.

The FTIR spectra of the synthesized materials are reported in Figure 3. For all the synthesized catalysts upon increase of the sodium aluminate content, additional stronger bands were detected in the 1400~1560 $cm^{-1}$ region; these bands are attributed to the presence of different carbonate species. Concomitantly, smaller signals due to the lowering of the carbonate's symmetry and consequent

activation of the $v_1$ (splitting of the site group) vibrational mode of carbonates are revealed at ~1100 and 964 $cm^{-1}$. Moreover, IR spectroscopy revealed the typical vibrations of the supports. Broad bands at 720 and 612 $cm^{-1}$ are well noticeable on titania -based catalysts, attributed to the vibration of $Ti^{4+}$ ion coordinated by oxygen ions. Vibration mode for adsorbed water was found with the band at 1642 $cm^{-1}$ [54]. Upon increase of the SA content the Ti-O bands become less resolved, with a progressive shift of the maximum from ~ 612 $cm^{-1}$ to 512 $cm^{-1}$ probably indicating a distortion of the bonding due to the SA introduction. The skeletal IR spectrum of γ-$Al_2O_3$ shows two broad and intense bands in the medium IR region at 588 $cm^{-1}$ and 799 $cm^{-1}$ as widely reported in the literature and attributed to the complex Al–O–Al bending stretching vibrations typical for defective spinels [55]. Absorbed $H_2O$ vibration band was detected at 1640 $cm^{-1}$. For hydrotalcite supported catalysts the three maxima at 473, 660 and 823 $cm^{-1}$ are assignable to the complex lattice vibrations of the Al-O and Mg-O bonds in the spinel defective cubic cell, typical of calcined hydrotalcite materials [56].

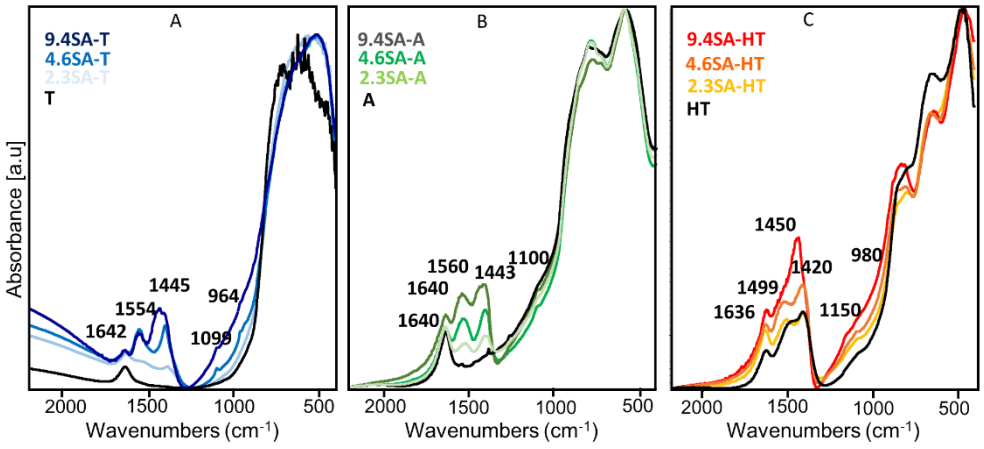


Figure 3: FTIR skeletal spectra (KBr pressed disks) of the calcined catalysts

Surface composition was studied by XPS, and a complete table related to the identification and quantification of the relevant species is reported in SI, Table S1, together will all the relevant high-resolution spectra (Fig. S1-S4). Insights related to the modification of the surface after the addition of sodium aluminate can be gained from the observation of the O 1s and C 1s peaks. High-resolution

spectra of O1s region for $TiO_2$ based catalysts (Fig. S1) was modified upon SA loading. The first feature at ~ 529 eV can be ascribed to lattice oxygen ($O_{lattice}$) [57] while the one at ~ 531 eV is classically attributed to hydroxyl groups (–OH) [58] of $TiO_2$ surface. Interestingly, the 531 eV component clearly increases upon introduction of $NaAlO_2$. This effect is also underlined by the fact that its concentration increases from 6.73% for $TiO_2$ to 15.51% for 9.7SA-T. Besides, considering the C 1s region (Fig. S4), the former feature at BE ~ 289 eV, related to carbonates species [59], becomes also more intense when the content of sodium aluminate is increased. Thus, correspondent increase of 531 eV O 1s, Na 1s and 289 eV C 1s components can be ascribed to the increasing presence of bicarbonates at the catalyst surface, in full agreement with drift analysis (vide infra). Nevertheless, looking also at the C 1s high resolution spectra (Fig. S4) of the other catalysts, the feature at BE ~ 289 eV becomes generally more intense when the content of sodium aluminate is increased. Correlation between this component and the SA content is reported in Figure 4A. Pristine HT showed a carbonate concentration of 2.78%. With respect to the other supports, this value is higher, despite no SA has been impregnated yet, this is because of the intrinsic basicity of the material. Instead, A-based catalysts revealed a slight increase of the carbonates surface concentration within the SA content. To sum up, upon sodium aluminate introduction, an overall, although moderate, increase of concentration of carbonates can be determined at the surface of all the catalysts.

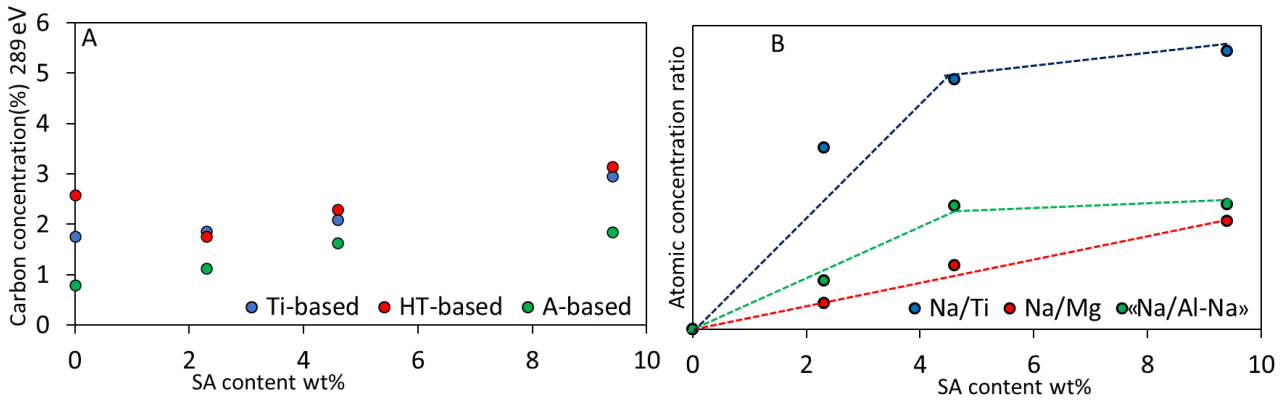

Figure 4: Surface characterization by XPS, leading to (A) an estimation of the surface carbon concentration arising from carbonates and (B) various relevant atomic ratios to depict the dispersion of sodium aluminate on the various supports, as a function of the loading. The dotted lines don't have any physical meaning and are merely guides to the eyes.

The sodium surface concentration was also assessed by XPS and used to obtain insights on its dispersion. In Figure 4B, different behaviours are observed for the three series of catalysts. On titania-based ones, the Na surface concentration increases strongly already at low loading, and then tends to level off, indicating that most of the active phase is likely concentrated at the surface. This aligns perfectly with the non-porous nature of the titania support which also develops relatively low specific surface area. For $Al_2O_3$ supported catalysts, a linear trend is observed up to 4.6%SA. Instead, for 9.4SA-A a less pronounced increase of Na/Al-Na ratio is observed. This effect can be correlated to a the pore filling of the support, leading to a considerable decrease in the specific surface area (SSA). In contrast, the hydrotalcite-based catalysts show a linear trend with the increase in SA content, suggesting that the support has a higher capability to accommodate and disperse the active phase.

$CO_2$-Temperature Programmed Desorption ($CO_2$-TPD) measurements provide access to quantitative and qualitative evaluation of basic sites [60]. Figure 5 shows the $CO_2$-TPD profiles for all the prepared catalysts. As often done in the literature [61–63], we propose to consider $CO_2$ molecules that are desorbed under 400°C as adsorbed on weak basic species. Then, the medium-strength basic sites are released between 400 and 650°C and desorption occurring after 650°C corresponds to strong basic sites. The basicity was dramatically modified by the introduction of sodium aluminate over the pristine supports. Over titania-based catalysts, a first peak was found with a maximum at 128 °C, due to the presence of weakly bonded $CO_2$ molecules at the surface. Upon increasing the SA content another contribution appeared at higher temperature (300-400 °C) and grew more intense. This feature is probably due to the $CO_2$ release by means of the weakest basic species. After 400 °C, stronger species are detected, such as monodentate or polydentate/bulk species [61]. On xSA-T catalysts, three desorption features can be described at 498-525 °C, ~600°C, and ~775 °C. A similar trend is observed over alumina-based materials, where a first peak appears in the range 120-136 °C.

This peak obviously grew in intensity (and shifted slightly towards higher temperatures) when SA content increased. Furthermore, this desorption tail was observed up to 300°C for all the xSA-A catalysts, disclosing the presence of medium strong basic species. In the high temperature region, two peaks were clearly detected, at 522 and 712 °C, revealing the presence of two well distinguished strong basic species. Finally, hydrotalcite-supported catalysts yielded more complex desorption profiles, basically due to the fact the support itself already shows a marked basic behavior. Interestingly, not only the basic sites quantity is enhanced (as underlined by the quantification reported in Table 1), but also the desorption temperatures are strongly modified upon addition of sodium aluminate. In fact, while the peak at 120 °C remained almost unchanged among the different catalysts, the more intense and broader desorption events occurring between 150 and 300°C (weak basic sites) were progressively suppressed upon SA increase. On the contrary, the peak found at 526 °C on the pristine support (medium-strength basic species), was increased in intensity and shifted to 560-570 °C, upon SA loading. At the same time a clear shoulder appeared around 600°C and a sharp peak at 708 °C is clearly detected for 9.4SA-HT while the highest temperature peak at 789 °C is almost unvaried. All in all, it is clear that sodium aluminate introduced different typologies and quantities of basic sites, depending on the support, and it strongly modifies their features depending on its loading.

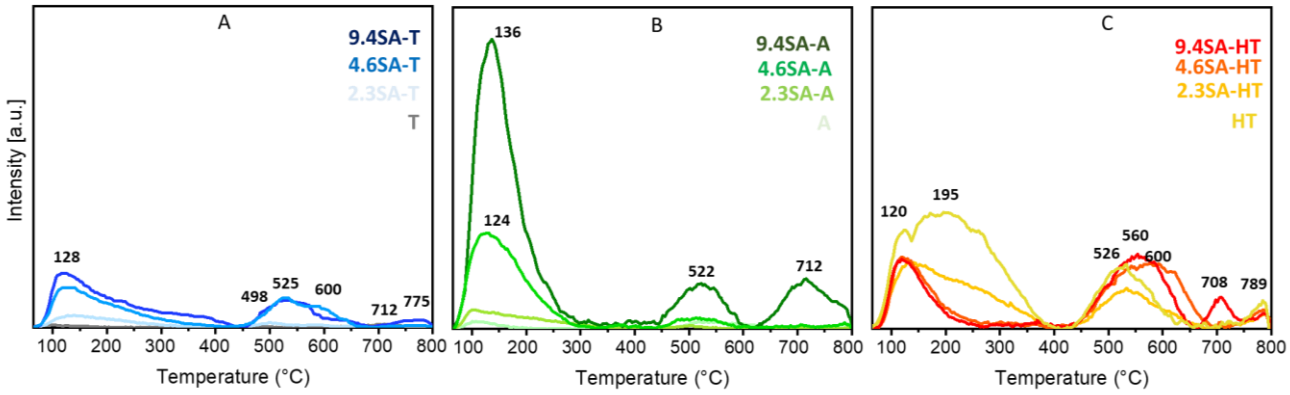


Figure 5: $CO_2$ TPD measures for the T-based catalysts, panel A, A-based catalysts, panel B, HT based catalysts, panel C.

Since the detection of carbonates is strictly related to the basic behavior of the catalysts surface, attempts to further describe the nature of these basic sites were made by DRIFTS analyses (Figure 6). First, spectra obtained immediately after a drying step at 120 °C (i.e. same conditions as when we use the catalysts in the transesterification reaction) are shown (continuous lines) to reveal the basic sites that are already occupied by atmospheric $CO_2$. Second, spectra obtained after a degassing step at 400 °C (dot lines) are reported, showing the carbonates that remain because they are more strongly bonded to the surface.

On titania-based catalysts, after the drying step, it is possible to detect the presence of surface OH-groups with a broad and intense band in the 3000-3600 $cm^{-1}$ region. These vibrations are not related to the carbonate species. However, at the same time, bicarbonate anions $HCO_3^-$ were found with the typical vibrations due to νOH, δOH and νC=O modes at 3695, 1640, 1460 $cm^{-1}$ [61]. Surprisingly, on 4.6SA-T and 9.4SA-T there was a lowering of the νOH vibration mode, producing a more evident peak at 3290 $cm^{-1}$. This is probably due to the distortion and rearrangement of the bicarbonates at the catalyst's surface when their amount is increased. Indeed, bicarbonates bands were drastically reduced after the degas at 400°C, meaning that they are weakly bonded to the surface (as suggested by literature [64]). The bonding of the carbonates to the catalysts surface caused some distortions in the doubly degenerate asymmetric C=O stretching vibration $\nu_3$, normally found in its free ion mode at 1415 $cm^{-1}$, causing a frequencies splitting, i.e. the so called $\Delta\nu_3$ splitting. The extent of this splitting is often used to discriminate among the different types of adsorbed carbonates in IR spectroscopy. Introducing sodium aluminate made the region between 1640 and 1370 $cm^{-1}$ more complex, with the rise of several absorption bands. Two vibration modes at 1570 and 1370 $cm^{-1}$ were detected, highlighting the presence of monodentate or chelated carbonates ($\Delta\nu_3$ ~100 up to 200) [65]. Looking at the spectra obtained after degassing (dotted lines), these bands remained stable, meaning that they are related to species adsorbed on relatively strong basic sites. With the increase of SA loading, the rise of the bands at 1826 and 1778 $cm^{-1}$ is ascribed to the formation of polydentate/bulk carbonate

species [66]. These species are still detectable after the degassing treatment meaning that they correspond to strongly adsorbed species. Finally, the vibration with a maximum around 1415 $cm^{-1}$ became more noticeable with the SA content increased, and it can be correlated with the shoulder in the range 1670-1640 $cm^{-1}$. Considering the wide $\Delta\nu_3$ (~ 250 $cm^{-1}$) these frequencies can be attributed to the presence of bridged carbonates [66].

In alumina-based catalysts, a similar trend was revealed. Firstly, on the bare support and on 2.3SA-A, surface hydroxyls and bicarbonate anions (3690 and 1645 $cm^{-1}$ respectively) were detected. As confirmed by their disappearance after the degas, these species are related to weakly bonded $CO_2$ molecules, thus to weakly basic sites. With the increase of SA content, monodentate (1385, 1570 $cm^{-1}$) and polydentate/bulk (1777 $cm^{-1}$) carbonate species clearly raised and remained relatively stable after the degassing step.

In hydrotalcite-supported catalysts, the basic properties of the pristine support were confirmed by the presence of complex and wide signals in the region 1350 $cm^{-1}$ – 1650 $cm^{-1}$. In agreement with TPD measurements, introducing the sodium aluminate strongly reduced the contribution of weak species, namely bridged carbonate species with vibrations at 1645 and 1375 $cm^{-1}$. In fact, their intensities generally dropped in the spectra recorded after the degas procedure, confirming their weak nature. On the contrary, SA introduction enhanced the contribution of stronger species such as monodentates in the region 1390-1570 $cm^{-1}$ (that are clearly still present on the spectra recorded after the degas step). Finally, even here, a component is detected at 1775 $cm^{-1}$ on 4.6SA-HT and 9.4SA-HT, suggesting the presence of polydentate/bulk species.

To sum up on the DRIFTS results, SA introduction deeply changes the basic properties of the catalysts, and the nature and extent of these modifications depend on the nature of the support. Loading SA generally led to the formation of bridged carbonates (weak strength), monodentate/ bidentate carbonates (medium strength), and polydentate species (high strength) on titania- and

alumina-based materials. Instead, on HT-based materials, SA introduction progressively formed medium and strong species at the expense of weak species.

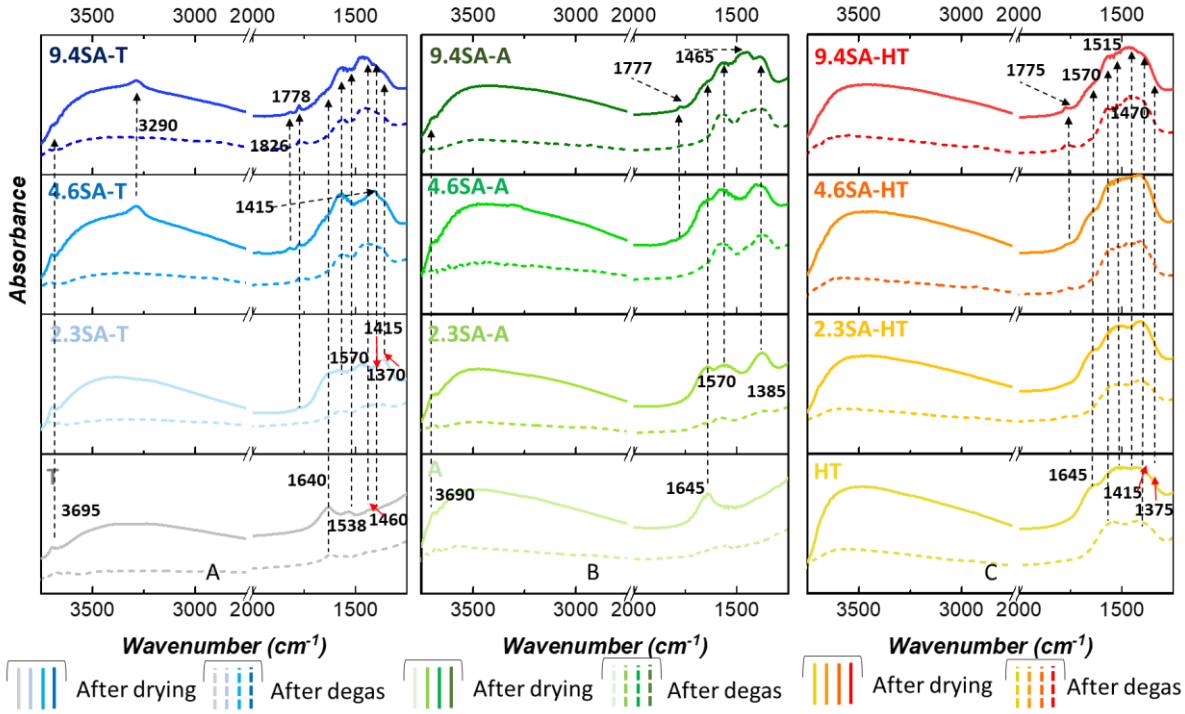


Figure 6: DRIFT spectra recorded immediately after the drying step (continuous lines) and after degassing at 400 °C (dotted lines) on titania-based catalysts (A), alumina-based catalysts (B) and hydrotalcite-based catalysts (C).

### *3.2 Catalytic behavior*

All catalysts have been tested in the transesterification of commercial sunflower oil with methanol, using a catalyst/oil mass ratio of 1.5 wt.% (Figure 7). Whatever the support used, the FAME yield (FY) clearly increased with the sodium aluminate content. Looking at the three catalysts with the highest SA loading, 9.4SA-T, 9.4SA-A and 9.4SA-HT reached a FY of 48%, 56%, 70% at 240 min, respectively. These results are in fully agreement with basic sites evaluation by TPD and DRIFTS

measures. In fact, the higher catalytic activity seems to be strictly related to the amount of medium and strong basic sites rather than the weak ones (vide infra and see also Table 1).

The potential contribution of homogeneous catalysis (leaching) was verified by hot filtration tests of 9.4SA-T, 9.4SA-A and 9.4SA-HT (Fig. S5). While over titania and alumina supported catalysts a minor homogeneous contribute cannot be excluded, HT based catalyst don't release any active species in the reaction media.

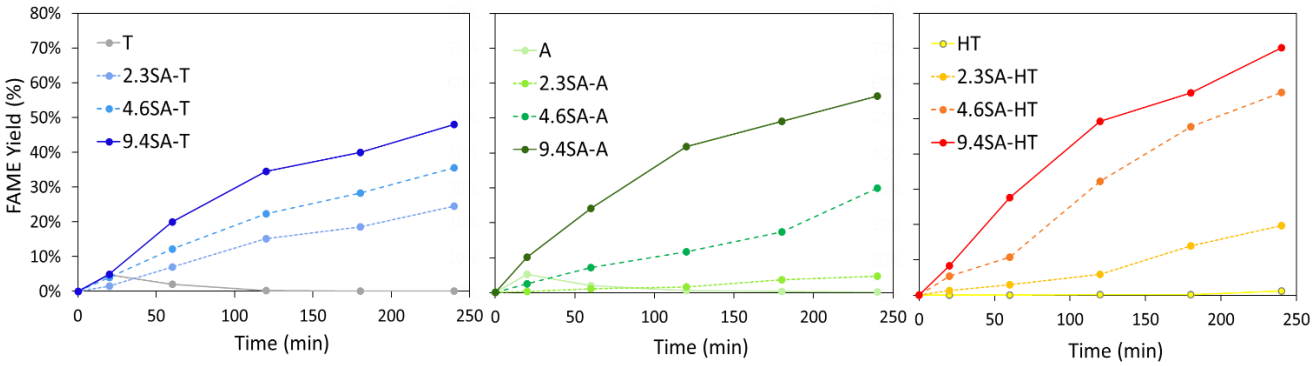


Figure 7: FAME Yield versus time plots, panels A, B, C refer to the comparison respect with the SA loading.

9.4SA-HT, with only a 9.4%wt of SA, i.e. 14.1 mg of $NaAlO_2$ loaded in the reactor, yields up to 70% were achieved after 240 min. Meanwhile, if pure sodium aluminate, which as previously identified as an outperforming catalyst among the heterogeneous ones [37], is used as the catalyst, i.e. 150 mg of $NaAlO_2$ loaded in the reactor, a FAME yield of 92% is reached after 240 min (Fig. S6). When the amount of sodium aluminate is adjusted to have the same active phase loading as in the test with the 9.4 wt.% catalysts (i.e.14.1 mg of pure SA) the yield was only 2%. Such value was slightly lower than expected but this can be explained by experimental bias such as small amount of powders sticking to the reactor walls under vigorous stirring. Importantly, the comparison of the tests done with the same amount of $NaAlO_2$, either pure or supported, shows unambiguously that the dispersion on a support results in enhancing markedly its catalytic activity (Fig. S7), and we attribute this to the formation of more basic surface sites.

The reusability of 9.4SA-HT was explored by testing the catalyst in two consecutive reactions (Fig. S8). When applying only washings and drying after the first run, the activity dropped markedly in the second run. However, when also applying a regenerative calcination the activity decreased only slightly, pointing to the presence of organic residues as the main cause for deactivation [37]. Further optimization of the regeneration for these catalysts is needed.

Our findings can be juxtaposed with existing literature that explored the utilization of supported sodium aluminate catalysts in transesterification reactions [67–71]. The catalytic data are reported in Table S2. Remarkably, 9.4SA-HT stands out among other catalysts reported. In fact, although it attains a 70% biodiesel yield within 4 hours while alternative catalysts achieve from 80% to 99% yield in 2-3 hours, the latter require either i) 3.5 to 20 times more catalyst in the reaction or ii) up to 10 times more sodium aluminate loading.

To further correlate catalytic activity and basicity, depending on the support nature, we plotted the FAME yield at 60 min (i.e. where conversion is still far from completion, but where significant amounts of FAME can be detected and quantified) versus the quantity of basic sites, expressed as mmol of $CO_2$ per g of catalyst, and classified as weak, medium-strong and strong (Fig. 8). Catalysts based on $TiO_2$ exhibited a consistent correlation between yield (ranging from 7% to 12%) and quantity of weak, medium, and strong basic sites (denoted in panels A, B, and C) for both 2.3 wt.% and 4.6 wt.% of SA. Intriguingly, while there are no significant changes in the relative abundance of basic sites when the loading is further increased to 9.4 wt%, the catalytic activity is higher (20%) for 9.4SA-T. In the case of alumina-based catalysts, a linear relationship emerges between the quantity of weak basic sites and the FAME yields (ranging from 1% to 24%). In the case of 9.4SA-A, a substantial increase in the quantity of medium and strong basic sites (combined increase from 0.037 to 0.203 $mmolCO_2/g_{cat}$) results in a significant jump in the FAME yield from 7% to 24%. This observation suggests that for 2.3SA-A and 4.6SA-A, the catalytic activity is primarily governed by weak basicity, leading to relatively low activity and correspondingly low FAME yields. Similarly,

over catalysts based on hydrotalcites (HT), the increasing FAME yield (from 3% to 28%) obtained when increasing the SA loading is concomitant with a decrease in the quantity of weak basic sites (reducing from 0.234 to 0.118 mmol$CO_2/g_{cat}$). This effect underscores the fact that these weak basic sites are not involved in the transesterification reaction. Conversely, the quantity of strong basic sites (panel C) notably increases (from 0.024 to 0.069 mmol$CO_2/g_{cat}$) with higher SA loading, significantly correlated with an increase in the FAME yield. In summary, the analysis demonstrates that the most influential factor for achieving a higher FAME yield is the presence of the strongest basic sites, i.e. those with desorption temperatures surpassing 650 °C.

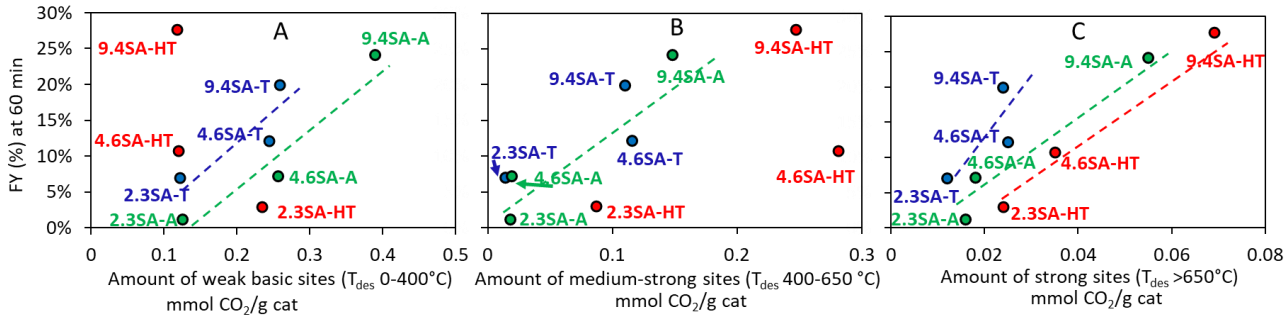


Figure 8: Comparison between the FAME yield qt 60 min and the amount (considering weak (A), medium (B) and strong (C) basicity) of basic sites respect to the SA loading, starting from 2.3, 4.6 and 9.4%, respectively.

In the end, it must be noted that the pristine supports with a much less pronounced basicity such as $TiO_2$ and $Al_2O_3$ did not catalyze the reaction in our experimental conditions. This is not surprising, considering that medium and strong basic sites are not detected by TPD and DRIFTS analyses. What was more surprising was the lack of activity for the calcined hydrotalcite, notoriously a quite active catalysts in base catalyzed transesterification [49,72]. We hypothesized that this was due the fact that a majority of the basic sites of HT were already occupied yet by environmental carbon dioxide. Thus, additional TPD experiments were conducted without any pre-treatment. Specifically, $CO_2$ adsorption was applied directly without prior degassing, and then followed by $CO_2$ desorption up to 400°C. Additionally, we conducted TPD measurements with fresh samples (not degassed, not saturated with $CO_2$) on both HT and 9.4SA-HT (Fig. 9). The resulting TPD profile allowed us to assess the amount

of $CO_2$ adsorbed from the environment on the catalyst surface. This represents catalytic sites that are already occupied and, therefore, inactive in the reaction. On the other hand, the TPD profile obtained after $CO_2$ adsorption is aimed to detect both the pre-existing $CO_2$ on the catalyst and the $CO_2$ introduced onto the available basic sites during saturation. These calculations are carried out as for previously mentioned TPD measures, however the values are not directly comparable because no degas pretreatment has been foreseen, so number of available catalytic sites can differ. By comparing the two curves, it is possible to determine the basic sites that are actually available for the transesterification reaction. Thus, although on pristine HT several weak and strong basic sites are present, only some of them are effectively available for catalysis i.e. total of 0.175 $mmolCO_2/g_{cat}$ and the amount of available medium and strong sites only accounts to 0.025 $mmolCO_2/g_{cat}$. In fact, most of them, as clearly shown in panel A, are weak species (maximum temperature of desorption = 120, 305, 328 °C). On the other hand, on 9.4SA-HT the total amount of effective sites is much higher, i.e. 0.247 $mmolCO_2/g_{cat}$) and a significant fraction (0.130 $mmolCO_2/g_{cat}$) corresponds to medium and strong basic sites, with peaks at 470, 561, 694 and 787 °C. To further understand which of these catalytic sites are more responsible for the catalytic activity, a TPD measurement was repeated on 9.4SA-HT and interrupted at 400 °C, and the resulting catalyst was subsequently tested in the transesterification reaction. In this way, only the sites that have been free through the desorption of $CO_2$ are available for the reaction. As expected, after such interrupted temperature-programmed desorption, the maximum yield obtained is strongly affected; almost half the original one at 240 min (Panel C, Figure 9). In fact, this phenomenon could be imputed to the fact that most of the strong basic sites are still poisoned and thus inactivated by $CO_2$. As confirmed by previous results, the population of the basic sites in the medium and strong region is the most responsible of a higher activity in the transesterification reaction.

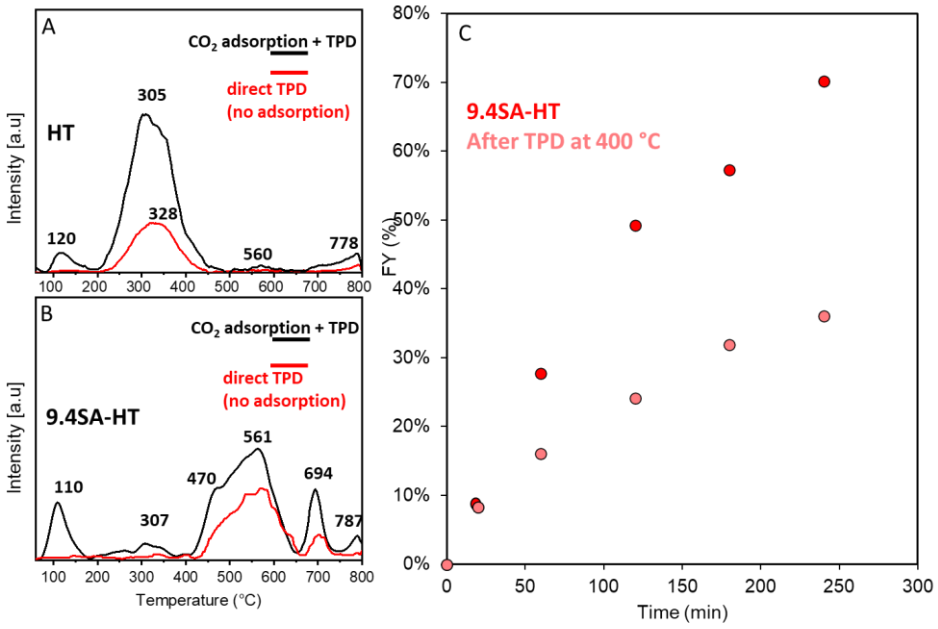


Figure 9: Panels A and B show TPD measures with only $CO_2$ adsorption and its desorption steps (black line), and only $CO_2$ desorption steps (red line) for HT and 9.4SA-HT. Panel C shows the FAME Yield for 9.4SA-HT after the selective poisoning of two different families of basic sites.

## 4 Discussion

From the results presented above, it appears that the intrinsic basicity of these catalysts depends both on the nature of the support and on the sodium aluminate loading. As shown in Figure 10, the two features are reciprocally influenced. Comparing the catalysts with the same nominal SA loading but different supports, a different distribution of basic species appears. Over titania based catalysts, sodium aluminate introduces more weak and medium species and this effect increases as the SA loading increases. Meanwhile, strong basic sites remain relatively low. Over alumina-based catalysts weak species are predominant on 2.3SA-A and 4.6SA-A while on 9.4SA-A medium and strong species are suddenly introduced. Looking at the hydrotalcite-based catalysts, sodium aluminate progressively suppresses weak basic sites while it majorly enhances medium strength species.

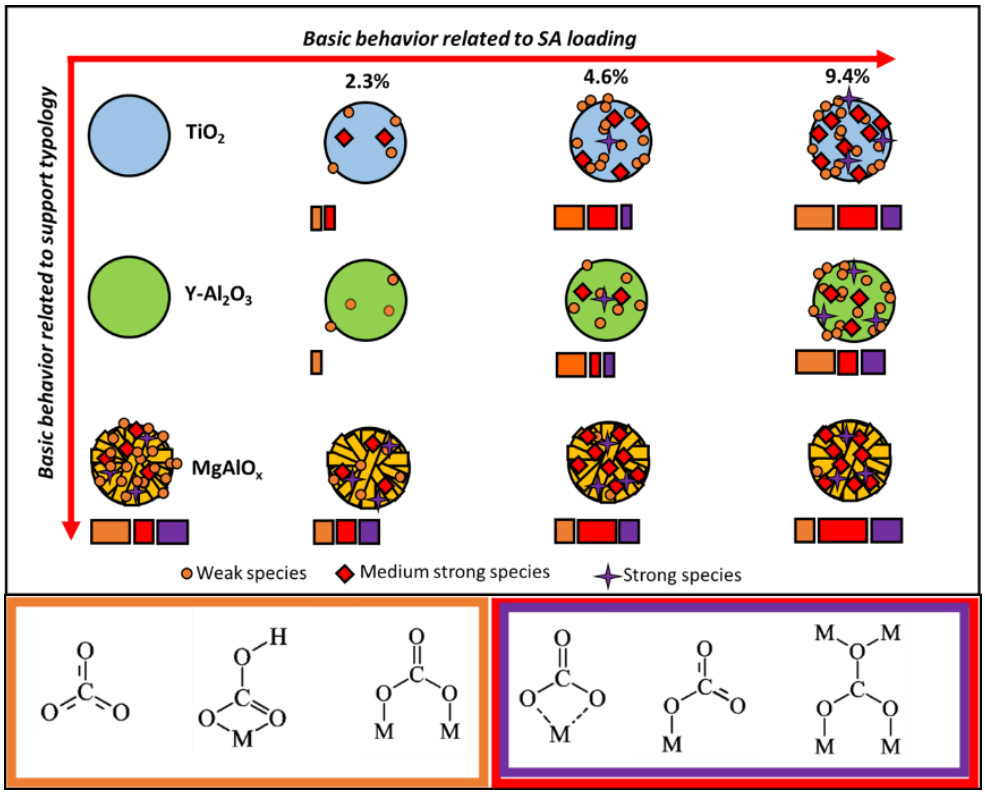


Figure 10: diagram depicting the relationship between the type of support, the amount of sodium aluminate introduced and their influence on the basic character of the catalysts.

The ionic structures of these supports show surface's defects that remain exposed and coordinatively unsaturated. To stabilize these high surface free energy points, reactions with molecules from the environment (e.g., water and $CO_2$) occur. Therefore, hydroxyl groups and surface carbonates are formed. On the oxide surface, Brønsted basic sites abstract a proton from a Brønsted acidic molecule. This process generates an anion that also needs to be stabilized by adsorption. In that sense, Brønsted basicity requires the presence of Lewis acidity to adsorb the conjugated base of the adsorbed acid molecule. Similarly, as depicted in Figure 11, when a Lewis base adsorbs a Lewis acid, neighboring Lewis acid sites stabilize the resulting anions (e.g. carbonates).

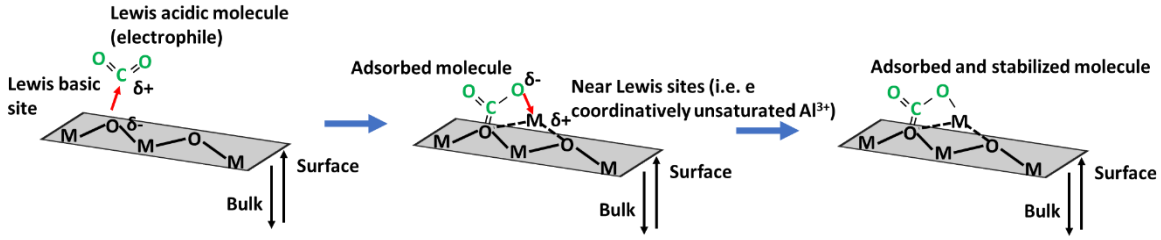

Figure 11: Scheme of stabilization deriving from acido-basicity of ionic oxides

Following the same reasoning, in the catalysts reported in this work, the presence of medium and strong basic sites is strictly related to $NaAlO_2$ or $Na_2O/Al_2O_3$ because they both have Brønsted basic species (unsaturated sites in Na-O bonds from Na in $NaO_4$ tetrahedra and/or $NaO_6$ octahedra) and Lewis acid sites (exposed $Al^{3+}$ sites in Al-O bonds of $AlO_4$ tetrahedra [55]). This proximity probably leads to the suppression of the weak basic species, as in hydrotalcite based catalysts, and to the emergence of a series of strong basic sites. Besides, on supports such as $TiO_2$ and $Al_2O_3$, the introduction of sodium aluminate radically changes the behavior, introducing both strong sites but also weak species deriving from the highly hydroxylated surface.

## 5 Conclusions

Sodium aluminate-based catalysts are promising material for the transesterification reaction of vegetal oil, in the perspective of the sustainable production of biodiesel. Hydrotalcite-supported catalysts are truly heterogeneous, and even with small quantities of sodium aluminate (i.e. 2.3% up to 9.4%) valuables FAME yields can be obtained. In particular, 9.4SA-HT shows the best catalytic activity achieving a 70% yield after 240 min of reaction, with a mere catalyst loading of 1.5% wt (with respect to the oil mass) in the reaction media. The effect of the support as well as the effect of SA loading have been investigated. A wide materials characterization revealed that over titania based catalysts, sodium aluminate introduces mostly weak (bicarbonates and bridged carbonates) and medium (bidentates and monodentates) basic sites. This effect increases as the SA loading increases but not linearly. Over alumina-based catalysts the same weak species are predominant on 2.3SA-A and 4.6SA-A, but on 9.4SA-A medium and strong species such as monodentates or polydentates are introduced. Looking at the hydrotalcite-based catalysts, sodium aluminate progressively suppresses the weak bridged carbonates while it majorly enhances medium strength species as monodentates or polydentates. Correlating the FAME yield at 60 min and the relative amount of the different types of

basic sites the predominant role of the strongest basic sites (i.e. desorption temperature > 650°C) is evident. Thus, monodentate and/or polydentate carbonates play a major role. However, the poisoning of basic sites by environmental $CO_2$ must be considered to understand the link between basicity and activity. Although 9.4SA-HT has fewer total basic sites than its pristine support (hydrotalcite), its effective amount of available strong sites is far higher than in latter. Thus, high catalytic performances for supported sodium aluminate catalysts are related to a combination of basic site strength and their effective availability during the reaction. Noting that environmental $CO_2$ has a relevant impact on catalytic activity, future works could study the impact of different storage atmospheres (i.e. dry air, inert, poisoned by $CO_2$) or tailored activation procedures on the amount of effectively available catalytic sites and on relative catalytic activity.

**Author contributions**

GP: Conceptualization, Investigation, Writing - Original Draft.
DPD: Supervision, Project administration, Funding acquisition, Review & Editing.

**Declaration of competing interest**

No potential conflict of interest was reported by the authors.

**Acknowledgments:** This study was carried out within the framework of the ADV_BIO project financed by the SPF Economie (Service Public Federal Belgium)" - Fonds de Transition Energetique, call 2019−2020 subsidies. Francois Devred is thanked for logistical assistance.

## References


[1] S. Bathmanabhan, S.N. Saragur Madanayak, Analysis and interpretation of particulate matter – PM10, PM2.5 and PM1 emissions from the heterogeneous traffic near an urban roadway, Atmos Pollut Res 1 (2010) 184–194. https://doi.org/10.5094/APR.2010.024.

[2] Emissions of air pollutants from transport — European Environment Agency. https://www.eea.europa.eu/data-and-maps/indicators/transport-emissions-of-air-pollutants-8/transport-emissions-of-air-pollutants-8 (accessed February 15, 2023).

[3] D.M. Alonso, J.Q. Bond, J.A. Dumesic, Catalytic conversion of biomass to biofuels, Green Chemistry 12 (2010) 1493–1513. https://doi.org/10.1039/c004654j.

[4] R. Pruszko, Biodiesel production, Bioenergy: Biomass to Biofuels and Waste to Energy (2020) 491–514. https://doi.org/10.1016/B978-0-12-815497-7.00023-3.

[5] B.R. Moser, Biodiesel production, properties, and feedstocks, In Vitro Cellular and Developmental Biology - Plant 45 (2009) 229–266. https://doi.org/10.1007/S11627-009-9204-Z.

[6] M.K. Lam, K.T. Lee, A.R. Mohamed, Homogeneous, heterogeneous and enzymatic catalysis for transesterification of high free fatty acid oil (waste cooking oil) to biodiesel: A review, Biotechnol Adv 28 (2010) 500–518. https://doi.org/10.1016/J.BIOTECHADV.2010.03.002.

[7] M. Ramos, A.P.S. Dias, J.F. Puna, J. Gomes, J.C. Bordado, Biodiesel Production Processes and Sustainable Raw Materials, Energies 2019, Vol. 12, Page 4408 12 (2019) 4408. https://doi.org/10.3390/EN12234408.

[8] S.K. Hoekman, A. Broch, C. Robbins, E. Ceniceros, M. Natarajan, Review of biodiesel composition, properties, and specifications, Renewable and Sustainable Energy Reviews 16 (2012) 143–169. https://doi.org/10.1016/J.RSER.2011.07.143.

[9] B. Thangaraj, P.R. Solomon, B. Muniyandi, S. Ranganathan, L. Lin, Catalysis in biodiesel production—a review, Clean Energy 3 (2019) 2–23. https://doi.org/10.1093/CE/ZKY020.

[10] A.E. Atabani, A.S. Silitonga, I.A. Badruddin, T.M.I. Mahlia, H.H. Masjuki, S. Mekhilef, A comprehensive review on biodiesel as an alternative energy resource and its characteristics, Renewable and Sustainable Energy Reviews 16 (2012) 2070–2093. https://doi.org/10.1016/J.RSER.2012.01.003.

[11] B. Changmai, C. Vanlalveni, A.P. Ingle, R. Bhagat, L. Rokhum, Widely used catalysts in biodiesel production: a review, RSC Adv 10 (2020) 41625–41679. https://doi.org/10.1039/D0RA07931F.

[12] A.P.S. Chouhan, A.K. Sarma, Modern heterogeneous catalysts for biodiesel production: A comprehensive review, Renewable and Sustainable Energy Reviews 15 (2011) 4378–4399. https://doi.org/10.1016/J.RSER.2011.07.112.

[13] A.F. Lee, K. Wilson, Recent developments in heterogeneous catalysis for the sustainable production of biodiesel, Catal Today 242 (2015) 3–18. https://doi.org/10.1016/J.CATTOD.2014.03.072.

[14] J. Gardy, E. Nourafkan, A. Osatiashtiani, A.F. Lee, K. Wilson, A. Hassanpour, X. Lai, A core-shell SO4/Mg-Al-Fe3O4 catalyst for biodiesel production, Appl Catal B 259 (2019) 118093. https://doi.org/10.1016/J.APCATB.2019.118093.

[15] V.K. Booramurthy, R. Kasimani, S. Pandian, B. Ragunathan, Nano-sulfated zirconia catalyzed biodiesel production from tannery waste sheep fat, Environmental Science and Pollution Research 27 (2020) 20598–20605. https://doi.org/10.1007/S11356-020-07984-1/TABLES/2.

[16] R. Liu, X. Wang, X. Zhao, P. Feng, Sulfonated ordered mesoporous carbon for catalytic preparation of biodiesel, Carbon N Y 46 (2008) 1664–1669. https://doi.org/10.1016/J.CARBON.2008.07.016.

[17] X. Tan, P. Sudarsanam, J. Tan, A. Wang, H. Zhang, H. Li, S. Yang, Sulfonic acid-functionalized heterogeneous catalytic materials for efficient biodiesel production: A review, J Environ Chem Eng 9 (2021) 104719. https://doi.org/10.1016/J.JECE.2020.104719.

[18] M. Saidi, M. Safaripour, F.A. Ameri, M.E. Jomeh, Application of sulfonated biochar-based magnetic catalyst for biodiesel production: Sensitivity analysis and process optimization, Chemical Engineering and Processing - Process Intensification 190 (2023) 109419. https://doi.org/10.1016/J.CEP.2023.109419.

[19] F. Esmi, V.B. Borugadda, A.K. Dalai, Heteropoly acids as supported solid acid catalysts for sustainable biodiesel production using vegetable oils: A review, Catal Today 404 (2022) 19–34. https://doi.org/10.1016/J.CATTOD.2022.01.019.

[20] W. Xie, X. Huang, Synthesis of biodiesel from soybean oil using heterogeneous KF/ZnO catalyst, Catal Letters 107 (2006) 53–59. https://doi.org/10.1007/S10562-005-9731-0.

[21] H. Ma, S. Li, B. Wang, R. Wang, S. Tian, Transesterification of Rapeseed Oil for Synthesizing Biodiesel by K/KOH/$\gamma$-$Al_2O_3$ as Heterogeneous Base Catalyst, JAOCS, Journal of the American Oil Chemists' Society 85 (2008) 263–270. https://doi.org/10.1007/S11746-007-1188-4.

[22] D. Salinas, P. Araya, S. Guerrero, Study of potassium-supported $TiO_2$ catalysts for the production of biodiesel, Appl Catal B 117–118 (2012) 260–267. https://doi.org/10.1016/J.APCATB.2012.01.016.

[23] L. Du, Z. Li, S. Ding, C. Chen, S. Qu, W. Yi, J. Lu, J. Ding, Synthesis and characterization of carbon-based MgO catalysts for biodiesel production from castor oil, Fuel 258 (2019) 116122. https://doi.org/10.1016/J.FUEL.2019.116122.

[24] D.E. López, J.G. Goodwin, D.A. Bruce, E. Lotero, Transesterification of triacetin with methanol on solid acid and base catalysts, Appl Catal A Gen 295 (2005) 97–105. https://doi.org/10.1016/J.APCATA.2005.07.055.

[25] A. Margellou, A. Koutsouki, D. Petrakis, T. Vaimakis, G. Manos, M. Kontominas, P.J. Pomonis, Enhanced production of biodiesel over MgO catalysts synthesized in the presence of Poly-Vinyl-Alcohol (PVA), Ind Crops Prod 114 (2018) 146–153. https://doi.org/10.1016/J.INDCROP.2018.01.079.

[26] M. Catarino, S. Martins, A.P. Soares Dias, M.F. Costa Pereira, J. Gomes, Calcium diglyceroxide as a catalyst for biodiesel production, J Environ Chem Eng 7 (2019) 103099. https://doi.org/10.1016/J.JECE.2019.103099.

[27] A.P. Soares Dias, J. Puna, J. Gomes, M.J. Neiva Correia, J. Bordado, Biodiesel production over lime. Catalytic contributions of bulk phases and surface Ca species formed during reaction, Renew Energy 99 (2016) 622–630. https://doi.org/10.1016/J.RENENE.2016.07.033.

[28] W. Xie, F. Wan, Basic ionic liquid functionalized magnetically responsive $Fe_3O_4$@HKUST-1 composites used for biodiesel production, Fuel 220 (2018) 248–256. https://doi.org/10.1016/J.FUEL.2018.02.014.

[29] W. Xie, C. Gao, J. Li, Sustainable biodiesel production from low-quantity oils utilizing $H_6PV_3MoW_8O_{40}$ supported on magnetic $Fe_3O_4$/ZIF-8 composites, Renew Energy 168 (2021) 927–937. https://doi.org/10.1016/J.RENENE.2020.12.129.

[30] L.R. V. da Conceição, L.M. Carneiro, D.S. Giordani, H.F. de Castro, Synthesis of biodiesel from macaw palm oil using mesoporous solid catalyst comprising 12-molybdophosphoric acid and niobia, Renew Energy 113 (2017) 119–128. https://doi.org/10.1016/J.RENENE.2017.05.080.

[31] C.T. Tracey, D.O. Shavronskaya, J. Shao, H. Yang, P. V. Krivoshapkin, E.F. Krivoshapkina, Heterogeneous carbon dot catalysts for biodiesel production: A mini review, Fuel 362 (2024) 130882. https://doi.org/10.1016/j.fuel.2024.130882.

[32] A.P.C. Teixeira, E.M. Santos, A.F.P. Vieira, R.M. Lago, Use of chrysotile to produce highly dispersed K-doped MgO catalyst for biodiesel synthesis, Chemical Engineering Journal 232 (2013) 104–110. https://doi.org/10.1016/J.CEJ.2013.07.065.

[33] J.R.D.O. Lima, Y.A. Ghani, R.B. Da Silva, F.M.C. Batista, R.A. Bini, L.C. Varanda, J.E. De Oliveira, Strontium zirconate heterogeneous catalyst for biodiesel production: Synthesis, characterization and catalytic activity evaluation, Appl Catal A Gen 445–446 (2012) 76–82. https://doi.org/10.1016/J.APCATA.2012.08.005.

[34] T.L. Kwong, K.F. Yung, One-step production of biodiesel through simultaneous esterification and transesterification from highly acidic unrefined feedstock over efficient and recyclable ZnO nanostar catalyst, Renew Energy 90 (2016) 450–457. https://doi.org/10.1016/J.RENENE.2016.01.028.

[35] Y.C. Zheng, X.H. Yu, J. Yang, Synthesis of CaO-$CeO_2$ catalysts by soft template method for biodiesel production, IOP Conf Ser Earth Environ Sci 69 (2017) 012048. https://doi.org/10.1088/1755-1315/69/1/012048.

[36] R. Estevez, L. Aguado-Deblas, F.M. Bautista, D. Luna, C. Luna, J. Calero, A. Posadillo, A.A. Romero, Biodiesel at the Crossroads: A Critical Review, Catalysts 2019, Vol. 9, Page 1033 9 (2019) 1033. https://doi.org/10.3390/CATAL9121033.

[37] G. Pampararo, D.P. Debecker, Sodium Aluminate-Catalyzed Biodiesel Synthesis, ACS Sustain Chem Eng 11 (2023) 10413–10421. https://doi.org/10.1021/ACSSUSCHEMENG.3C01692.

[38] S. Ramesh, F. Devred, D.P. Debecker, $NaAlO_2$-Promoted Mesoporous Catalysts for Room temperature Knoevenagel Condensation Reaction, ChemistrySelect 5 (2020) 300–305. https://doi.org/10.1002/SLCT.201904099.

[39] Y. Ning, S. Niu, S. Zhao, X. Zhang, Y. Zhang, K. Han, C. Lu, X. Zhang, Characterization of Dolomite Promoted by $NaAlO_2$ and Application as Catalyst in Transesterification by Response

Surface Methodology, ChemistrySelect 4 (2019) 9849–9856. https://doi.org/10.1002/SLCT.201902061.

[40] A. V. Agafonov, I.A. Yamanovskaya, V.K. Ivanov, G.A. Seisenbaeva, V.G. Kessler, Controlling micro- and nanostructure and activity of the $NaAlO_2$ biodiesel transesterification catalyst by its dissolution in a mesoporous γ-Al2O3-matrix, J Solgel Sci Technol 76 (2015) 90–97. https://doi.org/10.1007/S10971-015-3755-8/FIGURES/8.

[41] S. Ramesh, F. Devred, D.P. Debecker, $NaAlO_2$ supported on titanium dioxide as solid base catalyst for the carboxymethylation of allyl alcohol with DMC, Appl Catal A Gen 581 (2019) 31–36. https://doi.org/10.1016/J.APCATA.2019.05.017.

[42] S. Ramesh, F. Devred, L. van den Biggelaar, D.P. Debecker, Hydrotalcites Promoted by $NaAlO_2$ as Strongly Basic Catalysts with Record Activity in Glycerol Carbonate Synthesis, ChemCatChem 10 (2018) 1398–1405. https://doi.org/10.1002/CCTC.201701726.

[43] C.W. Huccrns, T.E. Gnern, Thermal Decomposition of Dawsonite, American Mineralogist 58 (1973) 548–550.

[44] P. Bénézeth, D.A. Palmer, L.M. Anovitz, J. Horita, Dawsonite synthesis and reevaluation of its thermodynamic properties from solubility measurements: Implications for mineral trapping of CO2, Geochim Cosmochim Acta 71 (2007) 4438–4455. https://doi.org/10.1016/J.GCA.2007.07.003.

[45] J.A. Kaduk, S. Pei, The Crystal Structure of Hydrated Sodium Aluminate, $NaAlO_2 \cdot 5/4H_2O$, and Its Dehydration Product, J Solid State Chem 115 (1995) 126–139. https://doi.org/10.1006/JSSC.1995.1111.

[46] M. Thommes, K. Kaneko, A. V. Neimark, J.P. Olivier, F. Rodriguez-Reinoso, J. Rouquerol, K.S.W. Sing, Physisorption of gases, with special reference to the evaluation of surface area and pore size distribution (IUPAC Technical Report), Pure and Applied Chemistry 87 (2015) 1051–1069. https://doi.org/10.1515/pac-2014-1117.

[47] A.K. Datye, G. Riegel, J.R. Bolton, M. Huang, M.R. Prairie, Microstructural characterization of a fumed titanium dioxide photocatalyst, J Solid State Chem 115 (1995) 236–239. https://doi.org/10.1006/JSSC.1995.1126.

[48] J. Yu, H. Yu, B. Cheng, M. Zhou, X. Zhao, Enhanced photocatalytic activity of $TiO_2$ powder (P25) by hydrothermal treatment, J Mol Catal A Chem 253 (2006) 112–118. https://doi.org/10.1016/J.MOLCATA.2006.03.021.

[49] A. Navajas, I. Campo, G. Arzamendi, W.Y. Hernández, L.F. Bobadilla, M.A. Centeno, J.A. Odriozola, L.M. Gandía, Synthesis of biodiesel from the methanolysis of sunflower oil using PURAL® Mg–Al hydrotalcites as catalyst precursors, Appl Catal B 100 (2010) 299–309. https://doi.org/10.1016/J.APCATB.2010.08.006.

[50] X.Y. Yang, L.H. Chen, Y. Li, J.C. Rooke, C. Sanchez, B.L. Su, Hierarchically porous materials: synthesis strategies and structure design, Chem Soc Rev 46 (2017) 481–558. https://doi.org/10.1039/C6CS00829A.

[51] M. Thommes, K. Kaneko, A. V Neimark, J.P. Olivier, F. Rodriguez-Reinoso, J. Rouquerol, K.S.W. Sing, IUPAC Technical Report Physisorption of gases, with special reference to the

evaluation of surface area and pore size distribution (IUPAC Technical Report), Pure Appl. Chem (2015) aop. https://doi.org/10.1515/pac-2014-1117.

[52] W. Lai, S. Yang, Y. Jiang, F. Zhao, Z. Li, B. Zaman, M. Fayaz, X. Li, Y. Chen, Artefact peaks of pore size distributions caused by unclosed sorption isotherm and tensile strength effect, Adsorption 26 (2020) 633–644. https://doi.org/10.1007/S10450-020-00228-1/TABLES/1.

[53] J.C. Groen, L.A.A. Peffer, J. Pérez-Ramírez, Pore size determination in modified micro- and mesoporous materials. Pitfalls and limitations in gas adsorption data analysis, Microporous and Mesoporous Materials 60 (2003) 1–17. https://doi.org/10.1016/S1387-1811(03)00339-1.

[54] T.K. Phung, L.P. Hernández, G. Busca, Conversion of ethanol over transition metal oxide catalysts: Effect of tungsta addition on catalytic behaviour of titania and zirconia, Appl Catal A Gen 489 (2015) 180–187. https://doi.org/10.1016/J.APCATA.2014.10.025.

[55] G. Busca, The surface of transitional aluminas: A critical review, Catal Today 226 (2014) 2–13. https://doi.org/10.1016/J.CATTOD.2013.08.003.

[56] F. Cavani, F. Trifirò, A. Vaccari, Hydrotalcite-type anionic clays: Preparation, properties and applications., Catal Today 11 (1991) 173–301. https://doi.org/10.1016/0920-5861(91)80068-K.

[57] M. Shen, M. Wang, Q. Wang, J. Tian, L. Zhang, L. Wang, J. Shi, A Ti-OH bond breaking route for creating oxygen vacancy in titania towards efficient $CO_2$ photoreduction, Chemical Engineering Journal 425 (2021). https://doi.org/10.1016/J.CEJ.2021.131513.

[58] Y. Zhang, Z. hongfei Xu, G. Li, X. Huang, W. eichang Hao, Y. Bi, D. Zhang, X. Huang, Y. Bi, D. Xu, W. Hao, G. Li, Direct Observation of Oxygen Vacancy Self-Healing on $TiO_2$ Photocatalysts for Solar Water Splitting, Angewandte Chemie International Edition 58 (2019) 14229–14233. https://doi.org/10.1002/ANIE.201907954.

[59] X-ray Photoelectron Spectroscopy (XPS) Reference Pages: C 1s - Carbonates. http://www.xpsfitting.com/2011/03/c-1s-carbonates.html (accessed February 16, 2023).

[60] M. Schmal, Heterogeneous Catalysis and its Industrial Applications, 2016. https://doi.org/10.1007/978-3-319-09250-8.

[61] G. Busca, Bases and basic materials in chemical and environmental processes. Liquid versus solid basicity, Chem Rev 110 (2010) 2217–2249. https://doi.org/10.1021/CR9000989/ASSET/CR9000989.FP.PNG_V03.

[62] R.P. Rocha, M.F.R. Pereira, J.L. Figueiredo, Characterisation of the surface chemistry of carbon materials by temperature-programmed desorption: An assessment, Catal Today 418 (2023) 114136. https://doi.org/10.1016/J.CATTOD.2023.114136.

[63] J.C. Védrine, Acid–base characterization of heterogeneous catalysts: an up-to-date overview, Research on Chemical Intermediates 2015 41:12 41 (2015) 9387–9423. https://doi.org/10.1007/S11164-015-1982-9.

[64] L. Smoláková, K. Frolich, I. Troppová, P. Kutálek, E. Kroft, L. Čapek, Determination of basic sites in Mg–Al mixed oxides by combination of TPD-$CO_2$ and $CO_2$ adsorption calorimetry: When the same basic sites are reported from both techniques?, J Therm Anal Calorim 127 (2017) 1921–1929. https://doi.org/10.1007/S10973-016-5851-6/FIGURES/7.

[65] D.P. Debecker, E.M. Gaigneaux, G. Busca, Exploring, Tuning, and Exploiting the Basicity of Hydrotalcites for Applications in Heterogeneous Catalysis, Chemistry – A European Journal 15 (2009) 3920–3935. https://doi.org/10.1002/CHEM.200900060.

[66] G. Busca, V. Lorenzelli, Infrared spectroscopic identification of species arising from reactive adsorption of carbon oxides on metal oxide surfaces, Materials Chemistry 7 (1982) 89–126. https://doi.org/10.1016/0390-6035(82)90059-1.

[67] Y. Ning, S. Niu, S. Zhao, X. Zhang, Y. Zhang, K. Han, C. Lu, X. Zhang, Characterization of Dolomite Promoted by $NaAlO_2$ and Application as Catalyst in Transesterification by Response Surface Methodology, ChemistrySelect 4 (2019) 9849–9856. https://doi.org/10.1002/SLCT.201902061.

[68] A. Chotchuang, P. Kunsuk, A. Phanpitakkul, S. Chanklang, M. Chareonpanich, A. Seubsai, Production of glycerol carbonate from glycerol over modified sodium-aluminate-doped calcium oxide catalysts, Catal Today 388–389 (2022) 351–359. https://doi.org/10.1016/J.CATTOD.2020.06.007.

[69] A. V. Agafonov, I.A. Yamanovskaya, V.K. Ivanov, G.A. Seisenbaeva, V.G. Kessler, Controlling micro- and nanostructure and activity of the $NaAlO_2$ biodiesel transesterification catalyst by its dissolution in a mesoporous $\gamma$-$Al_2O_3$-matrix, J Solgel Sci Technol 76 (2015) 90–97. https://doi.org/10.1007/S10971-015-3755-8/FIGURES/8.

[70] J. Keogh, G. Deshmukh, H. Manyar, Green synthesis of glycerol carbonate via transesterification of glycerol using mechanochemically prepared sodium aluminate catalysts, Fuel 310 (2022) 122484. https://doi.org/10.1016/J.FUEL.2021.122484.

[71] Y. Ning, S. Niu, Y. Wang, J. Zhao, C. Lu, Sono-modified halloysite nanotube with $NaAlO_2$ as novel heterogeneous catalyst for biodiesel production: Optimization via GA_BP neural network, Renew Energy 175 (2021) 391–404. https://doi.org/10.1016/J.RENENE.2021.04.135.

[72] D.G. Cantrell, L.J. Gillie, A.F. Lee, K. Wilson, Structure-reactivity correlations in MgAl hydrotalcite catalysts for biodiesel synthesis, Appl Catal A Gen 287 (2005) 183–190. https://doi.org/10.1016/J.APCATA.2005.03.027.